Modeling of plasma-controlled evaporation and surface condensation of Al induced by 1.06 and 0.248 μm laser radiations

V. I. Mazhukin and V. V. Nossov
Institute of Mathematical Modeling of RAS, 4a Miusskaya Square, 125047 Moscow, Russia

I. Smurov[a)]
Ecole Nationale d'Ingénieurs de Saint-Etienne, 58 rue Jean Parot, 42023 Saint-Etienne Cedex 2, France

(Received 27 June 2006; accepted 19 November 2006)

Phase transition on the surface of an aluminum target and vapor plasma induced by laser irradiation in the nanosecond regime at the wavelengths of 1.06 μm in the infrared range and 0.248 μm in the ultraviolet range with an intensity of 10^8–10^9 W/cm^2 in vacuum are analyzed. Special attention is paid to the wavelength dependence of the observed phenomena and the non-one-dimensional effects caused by the nonuniform (Gaussian) laser intensity distribution and the lateral expansion of the plasma plume. A transient two-dimensional model is used which includes conductive heat transfer in the condensed phase, radiative gas dynamics, and laser radiation transfer in the plasma as well as surface evaporation and back condensation at the phase interface. It was shown that distinctions in phase transition dynamics for the 1.06 and 0.248 μm radiations result from essentially different characteristics of the laser-induced plasmas. For the 1.06 μm radiation, evaporation stops after the formation of hot optically thick plasma, can occasionally resume at a later stage of the pulse, and proceeds nonuniformly in the spot area, and the major contribution to the mass removal occurs in the outer part of the irradiated region. Plasma induced by the 0.248 μm laser is colder and partially transparent since it transmits 30%–70% of the incident radiation; therefore evaporation does not stop but continues in the subsonic regime with the Mach number of about 0.1. The amount of evaporated matter that condenses back to the surface is as high as 15%–20% and less than 10% for the 1.06 and 0.248 μm radiations, respectively. For a beam radius smaller than ~100 μm, the screening and retarding effect of the plasma weakens because of the lateral expansion, thickness of the removed layer increases, and condensation after the end of the pulse is not observed. Comparison of the numerical and experimental results on the removed layer thickness has shown, in particular, the importance of accounting for the plasma effect to predict the correct trends for radiation intensity and beam radius. © *2007 American Institute of Physics*.
[DOI: 10.1063/1.2431951]

I. INTRODUCTION

The technique of material removal from a condensed target by the action of short high-power laser pulses usually referred to as *laser ablation* (LA) forms the basis for a number of technologies such as pulsed laser deposition (PLD), micromachining, structuring, or analysis of solid materials.[1–4] Along with the intensity and the pulse duration, the wavelength of laser radiation is a key parameter providing great flexibility to tailor this technique to suit specific tasks. Fast progress in laser equipment as well as emergency of advanced technologies have stimulated intensive studies in this field over a long period of time.

For metal targets, surface evaporation is always an important mechanism of material removal.[1,5] The process is characterized by the formation of a sharp phase boundary between the condensed and vapor phases and of a transient nonequilibrium layer adjacent to the boundary referred to as the Knudsen layer (KL). For equations of continuum mechanics a thin KL is a region of a strong discontinuity of thermo- and gas-dynamics variables.[6–10] The degree of nonequilibrium (the intensity) of evaporation is conveniently characterized by the Mach number on the outer boundary of the KL. Upon irradiation with a constant intensity in vacuum or in an environmental gas with a low counterpressure, evaporation proceeds with a sonic velocity $M=1$,[5,11] the material flux through the phase boundary is the highest, the process takes place under a strongest nonequilibrium, and the behavior of the condensed medium is independent of the state of the vapor region. Generally, subsonic evaporation $M<1$ is realized because of the counterpressure of the external gaseous medium[12–14] or the previously vaporized material,[15,16] and the processes in the condensed and vapor phases turn out to be interrelated.

Transition of a laser-irradiated matter from the condensed to the gaseous state can also proceed through other mechanisms different from surface evaporation: volumetric explosive boiling of the subsurface layer heated up to a near-critical temperature[17–19] or gas-dynamics outflow formed if the temperature and (or) pressure at the surface exceed(s) critical values.[20,21]

The problem of back condensation to the irradiated surface—the process opposite to surface evaporation—has been the concern of a number of recent studies analyzing

[a)]Electronic mail: smurov@enise.fr

laser ablation.[14,22–24] According to experimental data and analytical estimations,[22] the amount of evaporated matter that condenses on the surface after the end of the nanosecond laser pulse ranges from 10% for a monatomic vapor to 43% for large molecules. Progress in numerical studies of the back condensation is based in a great extent on the results in Refs. 25 and 26, which formulated boundary conditions at the condensed medium-vapor interface and tabulated relevant calculation data.

The course of laser-induced evaporation changes qualitatively if a plasma is formed in the evaporated matter. The most well-known consequence of the plasma formation is the absorption of incident laser radiation (screening effect) that affects the target heating and evaporation rate. The phenomenon was analyzed numerically by one-dimensional[23,27,28] (1D) and two-dimensional[29–31] models. Properties of the laser-induced plasma are known to be dependent on the radiation wavelength.[32–34] A comparative review of 1.06 and 0.308–0.199 μm UV laser plasmas presented in Ref. 4 shows that in the latter case the plasma appears to be colder and more transparent, allows for a greater removal of the target matter, and generates a moderate energy ion flux. With a nonuniform spatial distribution of the laser beam intensity the screening effect on the periphery of the plasma pattern can be weaker than in the center.[35]

A much less studied effect of plasma formation is the generation of a high counterpressure, which was demonstrated to be as much important as the screening effect:[36–38] high pressure of the plasma can not only decelerate but reverse the direction of the phase transition and leads to the back condensation onto the surface during the laser pulse despite the target temperature being much higher than the equilibrium boiling temperature.

Plasma formation is normally accompanied by emission of thermal radiation that can transport energy out of the system or redistribute it. This phenomenon represents an important source of information on plasma parameters. Studies of the radiation transfer upon the laser action of microsecond and nanosecond durations were performed in Refs. 39–44. In particular, thermal radiation generated by the hot outer layer of the plasma pattern was shown to deliver energy to the surface of the target.[39,41] According to Ref. 40 the radiative energy loss does not exceed 5%–10% of the total plasma energy for the microsecond action with the intensity of 5–50 MW/cm^2. For the nanosecond action, the increase of the radiation intensity from 10^9 to 2×10^{10} W/cm^2 augments the radiative loss from 10% to 60%.[43]

One more consequence of the plasma formation is a significant increase in gas-dynamics velocity in comparison with the nonionized vapor and the respective enhancement of lateral expansion. An example of the classification of plasma expansion regimes can be found in Ref. 45. Analysis of the transition from the one- to the three-dimensional (3D) expansion of ablation products upon the nanosecond action of neodymium-doped yttrium aluminum garneT (Nd-YAG) and ruby lasers with the intensity of 14 GW/cm^2 was performed in Ref. 46. The back condensation of evaporated matter outside the irradiation spot caused by the lateral expansion was observed in Ref. 21. The widening of the energy distribution zone at the surface due to the action of the thermal radiation of expanding plasma was pointed out in Ref. 47.

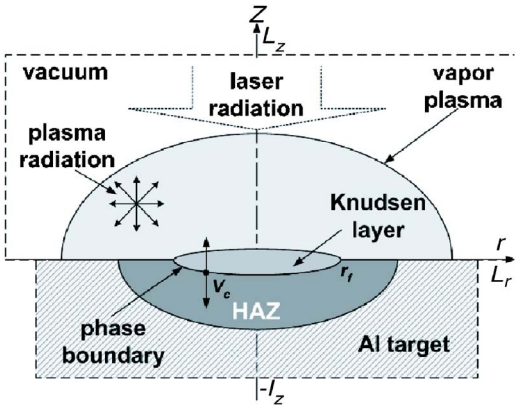

FIG. 1. (a) Setup and (b) reference frame of the problem.

The main objective of the present study is a comparative analysis of the phase transition on the surface of an aluminum target and of the properties of the vapor plasma induced by nanosecond laser radiation action at the wavelengths of 1.06 μm in the IR range and 0.248 μm in the UV range with an intensity of 10^8–10^9 W/cm^2 in vacuum. The paper is organized as follows. Section II gives a brief presentation of the model. In Sec. III, the principal features of the phase transitions are considered, and the effects of plasma screening, counterpressure, back condensation, and nonuniform intensity distribution are analyzed. Section IV is devoted to the structure of the plasma pattern, the effect of lateral expansion, and the role of thermal radiation. Qualitative comparison of the predicted results with the available experimental data and analytic estimations is given in the course of the presentation. In Sec. V a more detailed comparison with data on threshold intensities of plasma formation and thickness of the removed layer is performed along with some considerations on the dependence of the found regularities on the target material and environment parameters.

II. PROBLEM STATEMENT

The physical model used[37,38] accounts for the following phenomena: (i) surface heating of a metal target by laser radiation and conductive heat transfer; (ii) surface evaporation and back condensation; (iii) transfer and absorption of laser radiation in vapor plasma; (iv) gas-dynamics expansion, heating, and ionization of the plasma; and (v) generation and transfer of thermal radiation, Fig. 1(a). The processes were mathematically described in a coordinate system comoving with the target surface. Its origin was located in the center of the laser beam, the r axis coincided with the surface, and the z axis was directed along the outward drawn normal, Fig. 1(b).

A. Condensed medium

In the region $0<r<L_r$, $-l_z<z<0$ occupied by a condensed medium, Fig. 1(b), the heat transfer is described by the heat conduction equation:[48]

$$\rho_c C_p\left(\frac{\partial T_c}{\partial t}+V_c\frac{\partial T_c}{\partial z}\right)=\frac{1}{r}\frac{\partial}{\partial r}\left(rK\frac{\partial T_c}{\partial r}\right)+\frac{\partial}{\partial z}\left(K\frac{\partial T_c}{\partial z}\right), \quad (1)$$

where the subscript c denotes the condensed medium, T_c is the temperature, V_c is the velocity of the evaporation (condensation) front, and ρ_c, C_p, and K are the density, specific heat, and thermal conductivity. The absorption of the laser energy is described in the surface approximation; therefore the energy release term is not presented in Eq. (1) but in the interface boundary conditions (16) (see Sec. II C). The approach is valid since the thermal wave penetration depth $[K/(\rho C_p)\times\tau]^{1/2}\sim 10^{-4}$ cm is much greater than the depth of the absorption layer $(\kappa_C)^{-1}\sim 10^{-6}$ cm, for the considered target and laser pulse parameters.[49] Here τ denotes the laser pulse duration and κ_C is the absorption coefficient of the condensed medium.

The external boundaries of the region were assumed to be thermally insulated, the symmetry condition is fulfilled at $r=0$, and the initial target temperature is $T_0=300$ K. The target melting was excluded from consideration as it has a minor effect on the energy balance of the system because the latent melting heat is much smaller than the evaporation one. The model also does not account for hydrodynamic melt motion that insignificantly affects the surface phase transitions under nanosecond irradiation but would substantially complicate the model of the condensed medium and the computational algorithm.

B. Gaseous medium and plasma

The processes in the vapor region $0<r<L_r$, $0<z<L_z$, Fig. 1(b), were described by a system of radiative gasdynamics equations and the laser radiation transfer equation:[35,50]

$$\frac{\partial\rho}{\partial t}+\frac{1}{r}\frac{\partial}{\partial r}(r\rho u)+\frac{\partial}{\partial z}(\rho v)=0, \quad (2)$$

$$\frac{\partial(\rho u)}{\partial t}+\frac{1}{r}\frac{\partial}{\partial r}(r\rho u^2)+\frac{\partial}{\partial z}(\rho uv)=-\frac{\partial P}{\partial r}, \quad (3)$$

$$\frac{\partial(\rho v)}{\partial t}+\frac{1}{r}\frac{\partial}{\partial r}(r\rho uv)+\frac{\partial}{\partial z}(\rho v^2)=-\frac{\partial P}{\partial z}, \quad (4)$$

$$\frac{\partial(\rho e)}{\partial t}+\frac{1}{r}\frac{\partial}{\partial r}(r\rho ue)+\frac{\partial}{\partial z}(\rho ue)=-p\left[\frac{1}{r}\frac{\partial(ru)}{\partial r}+\frac{\partial u}{\partial z}\right]-\left(\frac{1}{r}\frac{\partial q_r}{\partial r}+\frac{\partial q_z}{\partial z}\right)+\left(\frac{\partial G}{\partial z}\right), \quad (5)$$

$$\operatorname{div}\boldsymbol{q}_\nu+c\kappa_\nu U_\nu=c\kappa_\nu U_{b\nu},\quad \boldsymbol{q}_\nu=-\frac{c}{3\kappa_\nu}\operatorname{grad}U_\nu,$$
$$U_{b\nu}=\frac{8\pi h\nu^3}{c^3[\exp(h\nu/kT)-1]}, \quad (6)$$

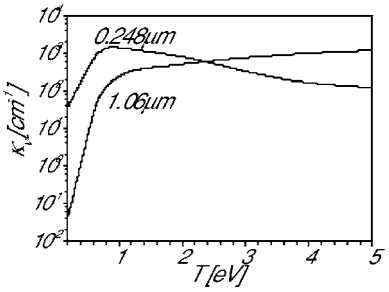

FIG. 2. Temperature dependency of plasma absorption coefficient $\kappa(T,\rho)$ at a fixed density $\rho=5\times10^{-3}$ g/cm^3 for the laser wavelengths of 1.06 and 0.248 μm.

$$\frac{\partial G^-}{\partial z}-\kappa G^-=0,\quad \frac{\partial G^+}{\partial z}+\kappa G^+=0,\quad G=G^-+G^+, \quad (7)$$

$$0<z<L_z,\quad 0<r<2r_f,$$

$$P=P(\rho,T), \quad (8)$$

$$e=e(\rho,T), \quad (9)$$

$$\kappa_\nu=\kappa_\nu(\rho,T,\nu), \quad (10)$$

where u and v are the components of the vapor velocity vector, ρ, P, and e are the density, pressure, and volume density of internal energy, $\boldsymbol{q}=\int_\nu \boldsymbol{q}_\nu d\nu=(q_r,q_z)$ is the thermal radiation flux, κ_ν is the spectral absorption coefficient, U_ν and $U_{\nu,\mathrm{eq}}$ are the volume density of plasma radiation and the blackbody radiation, and r_f is the laser beam radius. Equations (2)–(4) describe the gas movement in Euler approximation. The energy balance equation (5) accounts for the work of pressure, heating by the laser and thermal radiation, and neglects heat conduction. Equations (6) describe the radiation transfer in the diffusion approximation.[50,51] The laser radiation transfer equation (7) takes into account both the component incident on the target G^- and the reflected one G^+. The tabulated equations of the state [Eqs. (8) and (9)] were borrowed from Ref. 52. Absorption coefficients (10) were calculated by the approach of Ref. 53 based on the Hartree-Fock-Slater model. The equilibrium charge composition of the plasma and the excited state distribution were determined by the Saha-Boltzmann equations.[51]

The absorption coefficient $\kappa=\kappa(T,\rho)$ of the laser radiation was determined in the same way as the coefficient κ_ν.[53] Figure 2 shows two dependencies κ $(T,\rho=5\times10^{-3}$ g/cm$^3)$ related to the 1.06 and 0.248 μm radiations. For the 1.06 μm wavelength the inverse bremsstrahlung is the only absorption mechanism, and its contribution increases monotonically with temperature owing to the increase of the equilibrium concentration of electrons. For the 0.248 μm radiation the dependence is more complicated and includes the contribution of both the inverse bremsstrahlung and the photoionization.[23,51] The coefficient increases in the temperature range $T<1$ eV in which the photoionization of neutral atoms dominates. For higher temperatures $T>1$ eV the coefficient diminishes because nearly all neutrals are already ionized and the contribution of the photoionization decreases

rapidly. The comparison of the two curves shows that the 0.248 μm radiation heats plasma more effectively at low temperatures, while at the temperature $T>2$ eV absorption of the 1.06 μm radiation becomes more intensive.

The model neglects scattering of photons caused mainly by free electrons and characterized by a very small scattering cross section of $\approx 7\times 10^{-25}$ cm^2 (Refs. 42 and 51) (the so-called Thomson cross section). For an electron density of $\sim 10^{19}$ cm^{-3} typical for near-surface erosion plasma[4] it corresponds to a scattering coefficient of $\sim 10^{-5}$ cm^{-1} and is much smaller than the absorption coefficient, Fig. 2.

The system of equations (2)–(10) was supplemented with the following initial and boundary conditions:

$$t=t_0: \quad u=v=0, \quad T=T_0, \quad \rho=\rho_0, \quad 0\leqslant (r\times z)\leqslant (L_r\times L_z), \tag{11}$$

$$r=0: \quad u=0, \quad \partial\rho/\partial r=\partial v/\partial r=\partial P/\partial r=0, \quad q_r=0, \tag{12}$$

$$r=L_r: \quad p=p_0, \quad \rho=\rho_0, \quad u=v=0, \quad q_r=-cU/2, \tag{13}$$

$$z=L_z: \quad p=p_0, \quad \rho=\rho_0, \quad u=v=0, \quad q_z=-cU/2, \tag{14}$$

$$G^-\equiv G_0\exp[-(r/r_f)^2]\exp[-4(t/\tau-1)^2], \quad 0<r<2r_f,$$

$$z=0: \quad z=0{:}G^+=[1-A(T)]G^-, \quad 0<r<2r_f, \tag{15}$$

where τ is the laser pulse duration (full width at half maximum) and $A(T)$ is the surface absorptivity. Unlike for some other metals (Cu, Au, Ag, and Pt) absorptivity of the pure cold aluminum varies insignificantly in the spectral range of interest and falls within the range of 5%–10%;[4,54] therefore A was assumed to be independent of the wavelength. The temperature dependence was described by the expressions $A(T_c<T_m)=0.231$, $A(T_c>T_m)=0.64T_c^{0.4}$ taken from Ref. 29. According to the second relationship, the surface absorbs approximately half of the incident radiation at $T_c=6000$ K. The effect of a significant increase of the surface absorptivity (by three to five times) was also established in Refs. 4 and 55 for the 0.308 μm laser radiation with the peak intensity of 10^9 W/cm^2.

C. Interface boundary conditions

Boundary conditions at the interface relate six quantities: the front velocity V_c, the temperature T_c and the pressure P_c of the target surface with the temperature T, the density ρ, and the normal velocity v in the plasma at the external boundary of the KL. The conditions are formulated in different ways for the evaporation and condensation.[26] Independent of the direction of the phase transition the three conservation laws are fulfilled:

$$\lambda_c\frac{\partial T_c}{\partial z}=AG^-+L_v\rho_cV_c, \quad \rho_cV_c=\rho(V_c-v), \tag{16}$$

$$\rho_cV_c^2+P_c=\rho(V_c-v)^2+P,$$

where L_v is the heat of evaporation.

In the case of evaporation, two additional relationships of the Crout model were used:[56,57]

$$\frac{T}{T_c}=\frac{2\gamma M^2(m^2+1/2)^2}{(1+\gamma M^2)^2m^2t^2},$$

$$\frac{\rho}{\rho_{\text{sat}}}=\frac{tm^2(1+\gamma M^2)[\gamma M^2(m^2+1/2)]^{-1}}{\exp(-m^2)+\pi^{1/2}m[1+\text{erf}(m)]}, \tag{17}$$

$$M=v/\sqrt{\gamma RT}, \quad \rho_{\text{sat}}=P_{\text{sat}}/(RT_c),$$

$$P_{\text{sat}}=P_b\exp\left[\frac{L_v}{RT_c}\left(1-\frac{T_b}{T_c}\right)\right],$$

$$\left(1+\frac{3\gamma M^2-1}{\gamma M^2+1}\right)(m^2+1/2)^2-m^2(m^2+\alpha+3/2)=0,$$

$$\alpha=2t^2-2^{-1}\pi^{1/2}mt-1, \tag{18}$$

$$t=\frac{2m}{\pi^{1/2}}+\frac{1+\text{erf}(m)}{\exp(-m^2)+\pi^{1/2}m[1+\text{erf}(m)]},$$

where ρ_{sat} and P_{sat} are the saturated vapor density and pressure at the temperature T_c, R is the gas constant, γ is the adiabatic exponent (equal to 5/3 for monatomic vapor), P_b and T_b are the equilibrium pressure and temperature of boiling under normal conditions, and m, t, and α are the auxiliary variables of the Crout model coupled by relationships (18). The system of five relationships (16)–(18) has one free parameter, the Mach number, that depends on gas-dynamics flow conditions and was determined from Eqs. (2)–(5). It was assumed that the velocity v of the evaporation flow does not exceed the local sound velocity, $M\leqslant 1$.[6–8,26,56]

On reaching the inequality $P_{\text{sat}}<P$ the phase transition changes direction and evaporation is replaced by condensation $M<0$ that may take place in both the subsonic and supersonic regimes.[26] In the case of subsonic condensation $-1<M<0$, only one additional relationship was used:[37,38]

$$P/P_{\text{sat}}=0.95\exp(2.42|M|) \tag{19}$$

that approximates the tabular function $F_s(T/T_c,M)=P/P_{\text{sat}}$ (Refs. 25 and 58) and neglects the rather weak dependence of the F_s on the temperature ratio. For the supersonic regime $M<-1$, $P/P_{\text{sat}}>10$ all the three fluid parameters at the KL were determined from Eqs. (2)–(5).[26,38]

D. Algorithm of numerical solution

The differential model (1)–(19) was solved by the finite difference (FD) technique. The computational grid contained 50–100 nodes along the r axis in the region $0<r<L_r=5$ cm and was denser in the region of the laser spot, Fig. 1(b). The nonuniform grid along the z axis was separately

constructed in the condensed (l_z=0.01 cm, 40 nodes) and gaseous (L_z=10 cm, 100–200 nodes) regions. In both regions the grid became denser toward the target surface; the first steps were equal to 2×10^{-6} and 10^{-5} cm, respectively. The heat conduction equation with a convective term and temperature-dependent coefficients was approximated by a fully implicit difference scheme written on a five-point pattern and was solved by the alternating direction method with iterations.[59] A detailed description of the FD method used for radiative gas-dynamics equations is given in Refs. 40, 49, and 60. The computational algorithm of the problem as a whole took into account the interrelation of the processes and included three stages at each time step: solution of the equations in the gaseous state, calculation of relationships at the interface, and solution of the equation in the condensed medium. All the three stages were repeated in the outer loop.[36]

III. PHASE TRANSITIONS ON THE TARGET SURFACE

Let us turn now to the presentation and discussion of the results. In this section the regularities of the phase transition are considered induced by the 1.06 and 0.248 μm lasers with a fixed pulse duration τ=20 ns. The influence of the radiation intensity and the beam radius is analyzed by varying $G_0 \in 10^8-10^9$ W/cm^2 and $r_f \in 0.005-0.25$ cm [Eq. (14)] in respect to their reference values of 5×10^8 W/cm^2 and 0.025 cm. The intensity distribution is Gaussian in space that provides nonuniform irradiation conditions. The main analyzed variables of the predicted solution are the intensity of the transmitted laser radiation G_s, the surface temperature T_c, the plasma counterpressure $P_{\rm pl}$, the Mach number M, and the removed layer thickness H_v.

Parameters of the aluminum used in calculations are T_b=2720 K, P_b=1 bar, $L_v=1.1\times10^4$ J/g, and A_m=27 g/mol.[49] Values of the thermal conductivity, heat capacity, and density were specified taking into account the difference between the solid $T_c<T_m$ and liquid $T_c>T_m$ phases: K=2.37 and 0.75 W/(cm K), C_p=0.95 and 1.2 J/(g K), and ρ_c=2.7 and 2.33 g/cm^3 (the melting temperature T_m=933 K).[36,49]

The background density ρ_0 of 3×10^{-6} g/cm^3 was taken as corresponding to the background pressure $p_0=2\times10^{-3}$ bar.

A. Plasma transmission

The transmission coefficient is one of the most important optical characteristics of a plasma. It shows which part of the laser energy reaches the target and is spent for heating and removal of the material. Figure 3 represents time dependencies of this quantity $T_{\rm pl}=G^-(r,z=0)/G^-(r,z=L_z)$ taken in the beam center r=0 and at the boundary $r=r_f$ for the 1.06 and 0.248 μm radiations with $G_0=5\times10^8$ W/cm^2 and r_f=0.025 cm. The dashed lines in the figures indicate the action time and the shape of the laser pulse. For the 1.06 μm radiation the vapor remains transparent for some time after the onset of evaporation, Fig. 3(a). In the beam center, a sharp decrease of the transmission occurs at the instant $t^*\approx17$ ns with a minimum value of about 3% and corresponds

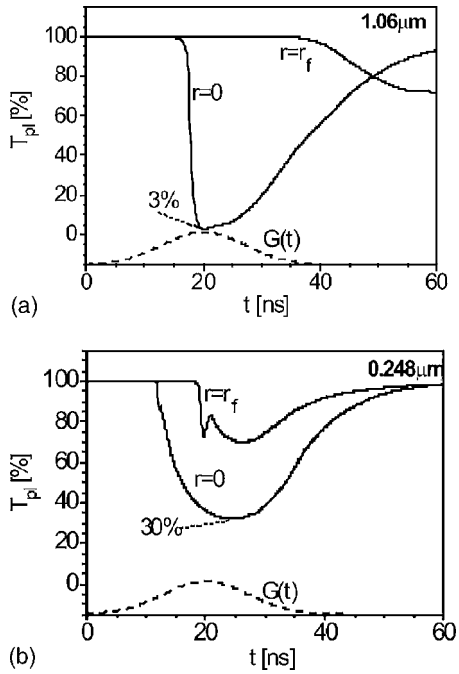

FIG. 3. Evolution of the plasma transmission $T_{\rm pl}(t,r)=G^-(t,r,z=0)/G^-(t,r,z=L_z)$ in the beam center r=0 and at the boundary $r=r_f$ for the laser wavelengths of (a) 1.06 μm and (b) 0.248 μm, $G_0=5\times10^8$ W/cm^2, and r_f=0.025 cm. Dashed line indicates the action time and the shape of the laser pulse.

to the initiation of the plasma. On the other hand, at the beam boundary the coefficient remains equal to about 100% for the whole period of irradiation, thus indicating that there is no plasma above this region of the target. For the 0.248 μm radiation the picture is qualitatively different, Fig. 3(b), r=0: the decrease of the transmission begins just after the onset of evaporation at $t^*\approx10$ ns but even at its minimum the coefficient does now fall below 30%. The dependence at $r=r_f$ is similar to the one in the center, but the plasma remains more transparent here and the minimum of transmission is as high as about 70%.

The obtained results are in rather good agreement with the available data on plasma transparency δ, $T_{\rm pl}=\exp(-\delta)$, measured for the similar action parameters $G_0=10^9$ W/cm^2 and τ=20–30 ns: $\delta=2-3$($T_{\rm pl}\approx5\%-10\%$) for the 1.06 μm (Ref. 17) wavelength and $\delta\approx0.25$ ($T_{\rm pl}\approx75\%$) for the 0.308 μm.[4,55] A more detailed comparison of the numerical and experimental results would be complicated by the heterogeneity of the plasma.

B. Action of the 1.06 μm laser radiation

Let us proceed with further considerations on the phase transition on the surface induced by the transmitted laser radiation. The time dependencies of the Mach number $M(t,r=0)$, the surface temperature $T_c(t,r=0)$, the saturated vapor pressure $P_{\rm sat}(t,r=0)$ and the plasma pressure $P_{\rm pl}(t,r=0)$ in the beam center ($r=0,z=0$) for the laser pulse with $G_0=5\times10^8$ W/cm^2 and r_f=0.025 cm are plotted in Fig. 4. The surface temperature that grows monotonically for the leading edge of the laser pulse lowers sharply at the instant of plasma formation before reaching the critical value of

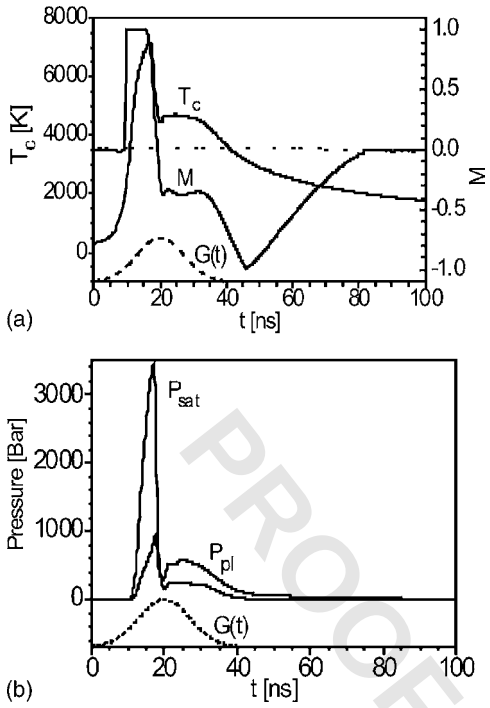

FIG. 4. Evolution of (a) the target surface temperature T_c and Mach number M. (b) Saturated vapor pressure P_{sat} and plasma pressure P_{pl} at the beam center $r=0$, $z=0$ for the laser wavelength of 1.06 μm, $G_0=5\times10^8$ W/cm^2, and $r_f=0.025$ cm.

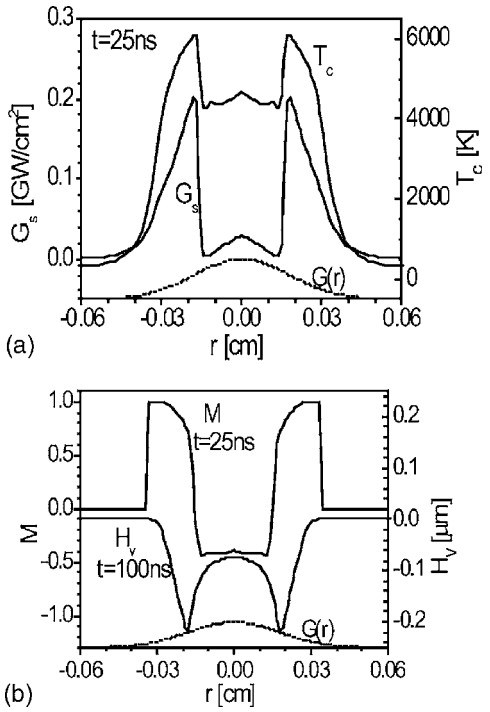

FIG. 5. Spatial distributions of (a) the transmitted intensity $G_s(t=25\ \mathrm{ns}, r)$ and the surface temperature $T_c(t=25\ \mathrm{ns}, r)$. (b) The Mach number $M(t=25\ \mathrm{ns}, r)$ and the removed layer thickness $H_v(t=100\ \mathrm{ns}, r)$ for the laser wavelength of 1.06 μm, $G_0=5\times10^8$ W/cm^2, and $r_f=0.025$ cm.

8000 K for aluminum,[49] Fig. 4(a). Simultaneously the Mach number starts to decrease from the $M=1$ level (the sonic velocity of the evaporated flux) to negative values $-1<M<0$ corresponding to the subsonic condensation. The vapor condensation is accompanied by the release of the heat of evaporation that compensates the conductive heat loss and, as a result, the temperature stabilizes at the level of approximately 4500 K, which is much higher than the equilibrium boiling temperature. The two stages of the phase transition are also well seen in Fig. 4(b) that presents the dependencies of the saturated vapor pressure P_{sat} and the counterpressure of the plasma P_{pl}. For the preplasma stage, the saturated vapor pressure is several times higher and the necessary condition of evaporation is fulfilled $P_{sat}>P_{pl}$. After the plasma formation the counterpressure increases while P_{sat} drops down following the cooling of the surface, and on reaching the condition $P_{sat}<P_{pl}$ the vapor outflow becomes completely suppressed and condensation begins.

The phase transition in the entire irradiated region is illustrated by the dependencies of the transmitted radiation intensities $G_s(t,r)$, the surface temperature $T_c(t,r)$, and the Mach number $M(t,r)$ at $t=25$ ns as well as the thickness of the removed layer $H_v(t,r)$ at the end of the computation $t=100$ ns, Fig. 5. The plots clearly show that the processes in the central and outer regions of the laser spot pass in different ways. In the central region $|r|<\approx r_f/2$ the plasma screens radiation that leads to a steplike drop of the G_s and T_c curves, Fig. 5(a). Note that the G_s value at the edge of the hollow corresponds to the threshold of the plasma formation for the 1.06 μm wavelength (see Sec. V A). Respectively, in the central region evaporation changes to condensation $M<0$, while in the outer region $|r|>\approx r_f/2$ the intensive evaporation with $M\approx1$ persists, Fig. 5(b). The total effect of the phase transition is given by the removed layer thickness obtained by integrating the front velocity: $H_v(r,t)=\int_0^t V_c(r,t')dt'$, Fig. 5(b). As evident from this plot, the contribution of the central region to the total mass removal is much smaller than the one of the zone near the beam boundary. The $H_v(r)$ should not be identified with the final shape of an ablation crater because the latter is substantially affected by hydrodynamics of the melted near-surface layer. The characteristic time of this transformation is longer than $r_f/u_{s,l}\sim100$ ns, where $u_{s,l}$ is the sound velocity of the liquid aluminum.

The dependencies of the Mach number $M(t)$ in the beam center, Fig. 6, illustrate how the found regularities of the phase transition vary for the different radiation intensities $G_0=2\times10^8-10^9$ W/cm^2 and beam radii $r_f=0.005-0.25$ cm. As seen in Fig. 6(a), with higher intensity the Mach number becomes positive again after the period of condensation, $M<0$; owing to the earlier formation of the plasma, it has time to partially restore its transparency before the end of the laser pulse and thus enables the evaporation to resume in the subsonic regime. The increase of the beam radius relative to the reference value of 0.025 cm has almost no effect on phase transition, Fig. 6(b), while for a smaller radius $r_f=0.005$ cm the difference is well noticeable: a small-volume amount of the evaporated matter expands very rapidly and the condensation after the laser pulse is not realized.

The $H_v(t)$ curves in Fig. 7(a) show evolution of the removed layer thickness with the different action parameters. The second rising interval of curves 1 (predicted for the smallest radius of 0.005 cm) and 2a (the highest intensity of

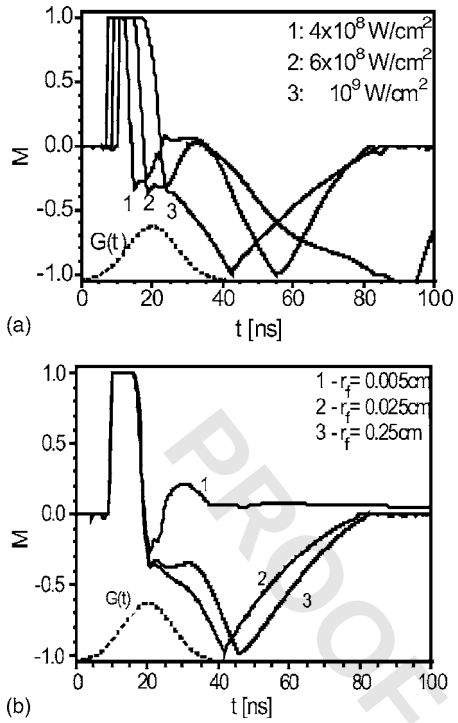

FIG. 6. Evolution of the Mach number $M(t,r=0)$ for (a) different peak intensities G_0, $r_f=0.025$ cm and (b) different beam radii, $G_0=5\times10^8$ W/cm^2 for the laser wavelength of 1.06 μm.

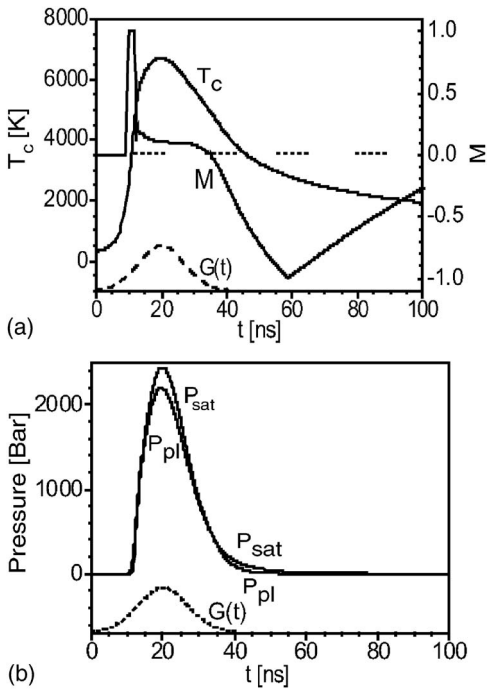

FIG. 8. Evolution of (a) the target surface temperature T_c and Mach number M. (b) Saturated vapor pressure P_{sat} and plasma pressure P_{pl} in the beam center $r=0$, $z=0$ for the laser wavelength of 0.248 μm, $G_0=5\times10^8$ W/cm^2, and $r_f=0.025$ cm.

10^9 W/cm^2) corresponds to the subsonic evaporation in the presence of the plasma and demonstrates that the mass removal can be substantial during this period. The falling intervals of all the four curves correspond to condensation and demonstrate that the amount of the evaporated matter condensed back to the surface in the beam center varies from 10% (curve 1) to nearly 50% (curves 2 and 3). The total fraction of the condensed matter obtained by integrating along the r coordinate was found to be smaller, 10%–20%. The portion condensed after the end of the pulse does not exceed several percent.

The final thickness of the removed layer for the different beam radii $H_v(r_f)$ is shown in Fig. 7(b), solid line. When decreasing the radius the removed layer first varies insignificantly and then, for the radii smaller than (~0.01 cm, begins to increase due to the lateral expansion of the plasma and reaches a value as high as 1–2 μm. A similar effect of the increased evaporation efficiency for smaller beam radii was communicated in Ref. 17. The $H_v(r_f)$ dependence predicted by the model that does not account for the plasma formation is also shown, Fig. 7(b), dashed line. In this case the beam radius variation does not produce substantial variation of the thickness (a slight slope observed is due to the back condensation): the expansion of the cold nonionized vapor proceeds with much lower velocity and has no time to manifest itself during the action even for the smallest beam radius considered.

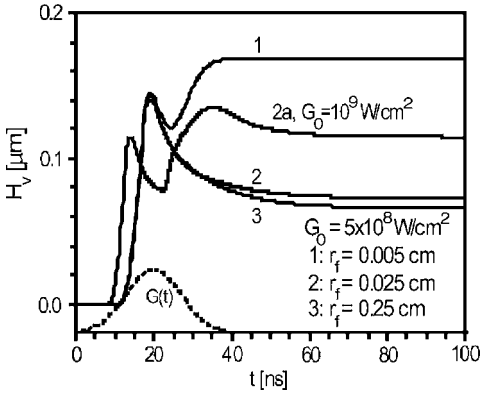

FIG. 7. (a) Evolution of the removed layer thickness at the beam center $H_v(t,r=0)$ for the different action parameters $G_0=5\times10^8$ W/cm^2, (1) $r_f=0.005$ cm, (2) $r_f=0.025$ cm, and (3) $r_f=0.25$ cm, and (2a) $G_0=10^9$ W/cm^2 and $r_f=0.025$ cm for the laser wavelength of 1.06 μm: (b) Removed layer thickness vs beam radius H_v (r_f) predicted with the account for the effect of plasma, solid line and neglecting plasma, dashed lines, $G_0=5\times10^8$ W/cm^2.

C. Action of the 0.248 μm laser radiation

Let us now analyze the phase transition induced by the 0.248 μm UV laser radiation, Figs. 8–10. The instant of the plasma formation $t^*=10$ ns is practically unnoticeable in the temperature plot but is well seen in the $M(t)$ dependence, Fig. 8(a). The stage of the sonic evaporation, $M=1$, turns out to be very short because of the early plasma formation. The most important difference as compared to the 1.06 μm action is that the evaporation does not stop after the plasma formation but continues in a subsonic regime $M\approx0.1$ and condensation begins only after the end of the laser pulse. The corresponding pressure curves are shown in Fig. 8(b): the difference between the saturated vapor and plasma pressures $P_{sat}-P_{pl}$ substantially decreases but remains positive after the plasma formation. Note also that the maximum plasma pressure is much higher for the 0.248 μm radiation, $P_{pl}\approx2000$ bars, in comparison with the one for the 1.06 radia-

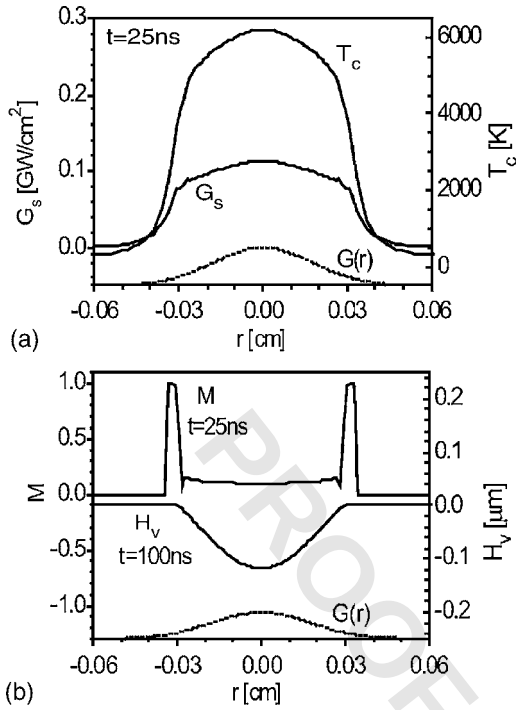

FIG. 9. Spatial distributions of (a) the transmitted intensity $G_s(t=25\ \mathrm{ns}, r)$ and surface temperature $T_c(t=25\ \mathrm{ns}, r)$. (b) The Mach number $M(t=25\ \mathrm{ns}, r)$ and removed layer thickness $H_v(t=100\ \mathrm{ns}, r)$ for the laser wavelength of 0.248 μm, $G_0=5\times10^8$ W/cm^2, and $r_f=0.025$ cm.

tion, $P_{pl}\approx700$ bars, Fig. 4(b). As shown in Sec. IV, the reason is that in the former case the hottest zone of the plasma locates just near the target surface in the maximum density region. However, the evaporated flow turns out to be able to overcome even this high counterpressure because of a high transmitted laser radiation flux that sustains high surface temperatures and, consequently, high saturated vapor pressures.

The dependencies of the phase transition characteristics on r coordinate, Fig. 9, also have a number of distinctions. In particular, the transmitted intensity G_s and the surface temperature T_c monotonically decrease from the center to the boundary of the spot, and their curves have a more "flat" shape as compared to the one of the incident pulse, Fig. 9(a). The phenomenon is explained by a higher transmission of the plasma in the outer region of the spot that partially compensates the lower intensity of the incident pulse. The subsonic evaporation proceeds at approximately the same rate $M\approx0.1-0.15$ throughout the spot region $|r|<r_f$, and the intensive evaporation with $M=1$ is observed only in the outermost part of the irradiation zone, Fig. 9(b). The final distribution of the removed layer thickness H_v has the shape of a hollow with smooth edges. The performed calculations showed that the intensity variation in the range of 10^8-10^9 W/cm^2 for the 0.248 μm laser radiation does not change qualitatively the course of the phase transition but only shifts the onset of evaporation, the plasma formation, and the transition to the subsonic regime to an earlier instant in time.[38]

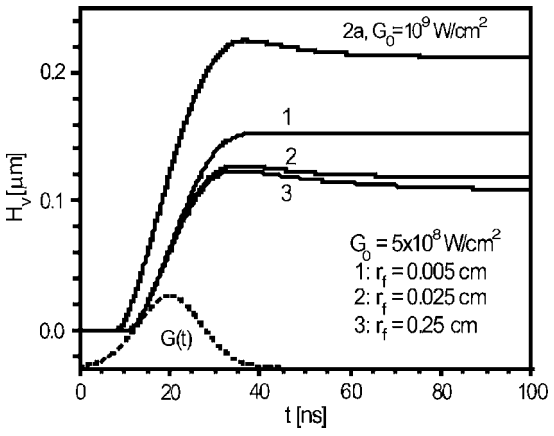

FIG. 10. Evolution of the removed layer thickness at the beam center $H_v(t, r=0)$ for the different action parameters $G_0=5\times10^8$ W/cm^2, (1) $r_f=0.005$ cm, (2) $r_f=0.025$ cm, and (3) $r_f=0.25$ cm, and (2a) $G_0=10^9$ W/cm^2 and $r_f=0.025$ cm for the laser wavelength of 0.248 μm.

It is well seen from the removed layer thickness H_v curves in the beam center obtained for different action parameters, Fig. 10, that this quantity monotonically increases until the end of the laser pulse owing to the unceasing evaporation and only then yields place to the condensation. The total fraction of the condensed material decreases with decreasing the beam radius from 10% for $r_f=0.25$ cm to 4% for $r_f=0.025$ cm while for the radii smaller than ~0.01 cm the condensation is not realized. Note that the value of 10% corresponding to the greatest radius coincides with the result of Ref. 22 for condensation of the monatomic vapor produced by the nanosecond UV laser action with the fluency of 2 J/cm^2 in air.

On the whole, the presented results show that the surface phase transitions induced by the 1.06 and 0.248 μm radiations have a number of differences. In the former case the screening and retarding effect of the plasma is strong in the central part of the beam that stops evaporation and provokes a partial recondensation of the evaporated substance and is practically unnoticeable near the beam boundaries. In the latter case the plasma effect is weaker, it slows down evaporation but does not suppress it completely, and manifests itself over the entire surface of the irradiation spot.

IV. PLASMA CHARACTERIZATION

This section considers characteristics of the vapor plasmas induced by the 1.06 and 0.248 μm laser radiations. In Sec. IV A the temperature distribution $T(r,z)$ and the shape of the plasma pattern are compared for the effect of $G_0=5\times10^8$ W/cm^2. In Sec. IV B the features of the pattern expansion are given as predicted for the different beam radii and, finally, in Sec. IV C the role of the plasma thermal radiation is analyzed by means of comparison of the plasma q_z and laser G^- radiation fluxes.

A. Plasma temperature and pattern structure

Two-dimensional distributions of the plasma temperature at the instant of 25 ns for the action parameters $G_0=5\times10^8$ W/cm^2, $r_f=0.025$ cm, and the two wavelengths of 1.06 and 0.248 μm are shown in Figs. 11(a) and 11(b). At these parameters the plasma temperature is approximately the same—about 3–4 eV—for both wavelengths, but the lo-

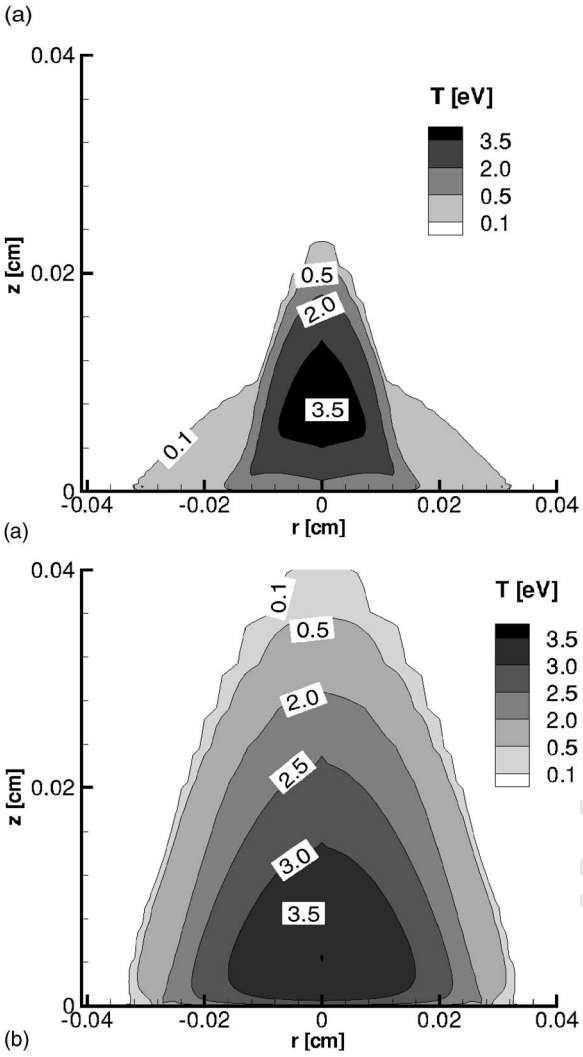

FIG. 11. Contour plot of the plasma temperature distribution $T(t=25\ \mathrm{ns}, r, z)$ for the laser wavelengths of (a) 1.06 μm and (b) 0.248 μm, $G_0=5\times10^8$ W/cm^2, and $r_f=0.025$ cm.

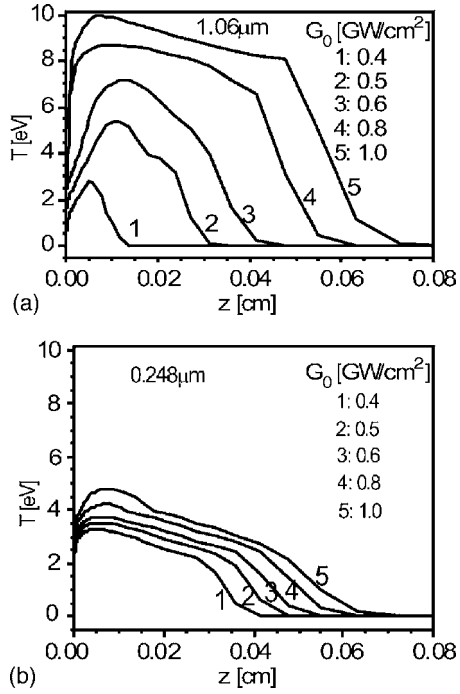

FIG. 12. Temperature distribution on the beam axis $T(t=25\ \mathrm{ns}, r=0, z=0)$ for different intensities G_0 and the laser wavelengths of (a) 1.06 μm and (b) 0.248 μm and $r_f=0.025$ cm.

cation of the hottest region, the "core," is different: it is shifted toward the forefront of the pattern for the 1.06 μm radiation and is adjacent to the target surface for the UV action. It was established that the position of the core coincides with the region where the incident laser radiation is released [see Fig. 15, $G^-(z)$ plot]. The size of the plasma pattern conditionally bounded by the isotherm $T=0.5$ eV is greater in both directions for the 0.248 μm radiation. For the z direction it is explained by the earlier instant of the plasma formation, and for the r direction by the wider region of the plasma initiation. Additionally, the "wings" of the pattern are well seen for the 1.06 μm radiation, Fig. 11(a), bounded by the isotherm of 0.1 eV. The wings consist of the nonionized vapor produced by the evaporation from the outer region of the irradiation spot, have the temperature of 0.1–0.3 eV, and are characterized by a much lower velocity of the gas-dynamics expansion than the one of the plasma core.

The distributions of the plasma temperature at the beam axis $z=0$ for different radiation intensities are shown in Fig. 12. The 1.06 μm radiation leads to a substantial plasma heating with the maximum temperature as high as 10 eV reached for the action of 10^9 W/cm^2. For the 0.248 μm radiation the efficiency of the laser heating drops down as soon as the temperature of 2–3 eV is reached because of the weakening of photoionization and the low efficiency of the inverse bremsstrahlung effect for the short wavelength radiation. As a result, the increase in radiation intensity does not lead to further plasma heating.

The observed distinction between the typical plasma temperatures for the IR and UV laser radiations is consistent with the data on plasma temperature cited in Ref. 4. In particular, the plasma of 10 eV was observed for the nanosecond action of 1.06 μm laser[17] while the measured temperature did not exceed 2–3 eV for the 0.308 μm irradiation of approximately the same duration and intensity.[55,61] The decrease in steady-state plasma temperature with the increasing energy of laser quantum for the microsecond pulses was discussed in Ref. 33.

B. Expansion of the plasma pattern

The plasma expansion for the 1.06 μm radiation is illustrated in Fig. 13, showing distributions of the plasma pressure (contour plots) and the gas-dynamics velocity (vector plots) for the different beam radii at two instants of time: $t=30$ ns (the final stage of the laser pulse) $r_f=0.25$ cm (a), $r_f=0.025$ cm (b), and $r_f=0.005$ cm (c) and $t=60$ ns (the stage of inertial expansion) $r_f=0.25$ cm (d), $r_f=0.025$ cm (e), and $r_f=0.005$ cm (f). For interpretation of the results a nondimensional time variable is introduced: $t'=(t-t^*)/t_{gd}$, $t_{gd}=r_f/u_{s,pl}$, where $u_{s,pl}$ is the sound velocity of the plasma.[45,46] The $t'\ll1$ and $t'\gg1$ cases correspond to the one- and three-dimensional expansions, respectively, while the $t'\approx1$ relates to the intermediate regime. The results in

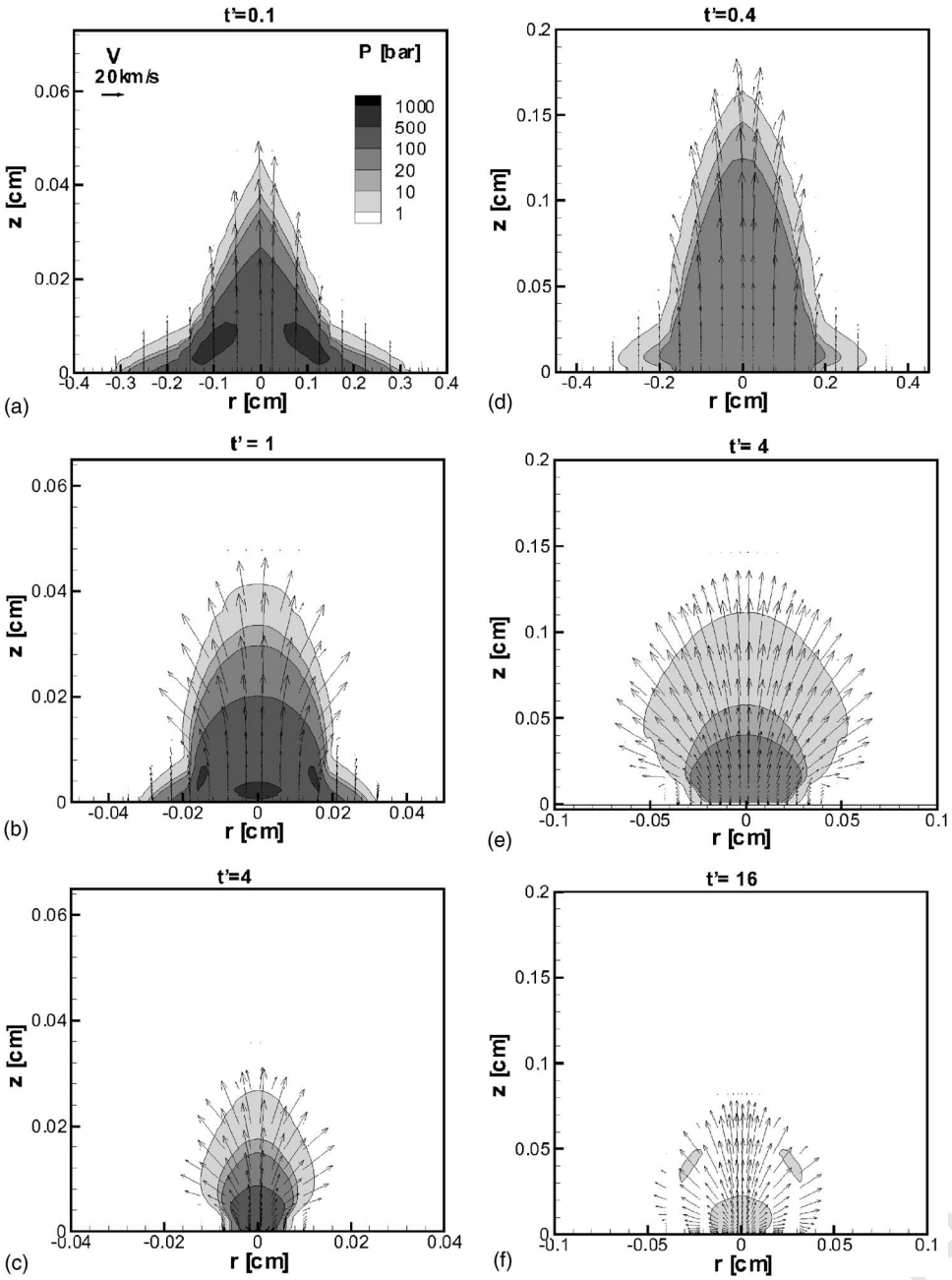

FIG. 13. Distributions of the pressure $P(t,r,z)$ (contour plot) and velocity vector $V(t,r,z)$ at the instants of $t=30$ ns (a) $r_f=0.25$ cm, (b) $r_f=0.025$ cm, and (c) $r_f=0.005$ cm and $t=60$ ns, (d) $r_f=0.25$ cm, (e) $r_f=0.025$ cm, and (f) $r_f=0.005$ cm, for the laser wavelength of 1.06 μm and peak intensity $G_0=5\times10^8$ W/cm^2. Nondimensional time variable is defined as $t'=(t-t^*)/t_{gd}$, $t_{gd}=r_f/u_{s,pl}$, where t^* is the instant of plasma formation and $u_{s,pl}$ is the sound velocity of the plasma.

Figs. 13(a) and 13(d), predicted for the greatest beam radius correspond to the 1D expansion at both instants, $t'=0.1$ and 0.4. The expansion of the central part of the plasma in the z direction proceeds faster than the expansion of the colder wings leading to the formation of a "spacecraftlike" pattern. For the reference radius of 0.025 cm, Figs. 13(b) and 13(e), a noticeable lateral expansion begins at the end of the action, $t'=1$, and becomes clearly 3D after the end of the pulse, $t'=4$. The central part of the pattern expands mainly away from the target surface and in the lateral direction around the wings. Such an expansion explains, in particular, why the condensation is negligible after the laser pulse. For the smallest radius, Figs. 13(c) and 13(e), the expansion is three dimensional at both instants $t'=4$ and $t'=16$ that manifests itself in the weaker screening and the retarding effect of the plasma.

For the 0.248 μm radiation, the regularities of the plasma expansion are in general similar to the ones presented above, Fig. 14, but the pattern structure is somewhat simpler owing to a more uniform vapor flow from the surface. The distinction of this regime is that the central part of the pattern expands both away and toward the surface, Fig. 14(b), leading to a rather intensive condensation after the end of the pulse.[38]

C. Plasma thermal radiation

As it was shown in the studies dealing with the microsecond laser action, thermal radiation of plasma occasionally turns out to be the main mechanism of energy delivery to the target surface.[27,36,41] Let us consider if this phenomenon takes place upon irradiation by nanosecond pulses.

The dependences of the thermal radiation flux $q_z(z)$, the incident laser radiation $G^-(z)$, the temperature $T(z)$, and the density $\rho(z)$ along the beam axis $r=0$ at the instant $t=25$ ns are plotted in Fig. 15 for the 1.06 μm (a) and

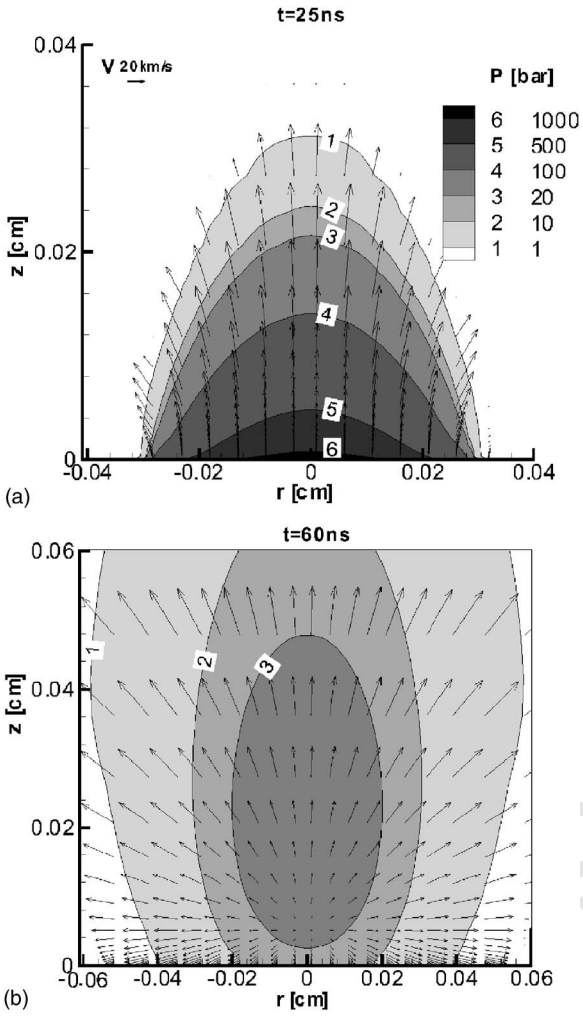

FIG. 14. Distributions of the pressure $P(t,r,z)$ (contour plot) and velocity vector $V(t,r,z)$ at the instants of (a) 25 ns and (b) 60 ns for the laser wavelength of 0.248 μm, $G_0=5\times10^8$ W/cm^2, and $r_f=0.025$ cm.

0.248 μm (b) radiations with $G_0=5\times10^8$ W/cm^2 and $r_f=0.025$ cm. For the 1.06 μm irradiation the maximum of the radiation flux is reached in the highest temperature region and is directed away from the target, $q_z>0$, Fig. 15(a). The flux toward the target $q_z<0$ is much weaker and attenuates further in the colder near-surface layer. The described picture of the radiation field is similar to the two-layer model of a plasma proposed in Ref. 41. The principal distinction, however, consists in that the laser radiation flux exceeds the flux of the thermal radiation by approximately an order of magnitude. The weakness of the plasma radiation is due to its relatively low temperature and the small effective thickness of the emitting layer which is of the order of the beam radius $\sim r_f$ (see also the analysis of Fig. 17).

The distinction of the thermal radiation field for the 0.248 μm radiation is related to a different structure of the plasma pattern: the flux toward the target is formed just near the surface and turns out to be much higher than the one for the 1.06 μm radiation, Fig. 15(b). However, the attenuation of the laser flux is also much weaker in this case, therefore the contribution of the plasma radiation to the total energy flux at the surface remains negligible.

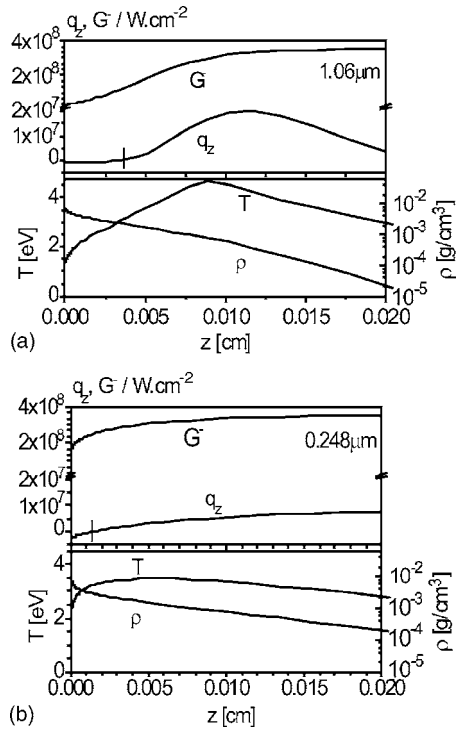

FIG. 15. Distributions of laser intensity G^-, z component of the thermal radiation flux q_z, plasma temperature T, and density ρ on the beam axis $r=0$ at the instant $t=25$ ns, for the laser wavelengths of (a) 1.06 μm and (b) 0.248 μm, $G_0=5\times10^8$ W/cm^2, and $r_f=0.025$ cm. Small vertical lines mark the right boundary of the zone where q_z is negative and plasma emits radiation towards the target.

The proportion of the laser and thermal radiation fluxes is illustrated by its dependencies on r coordinate, $t=25$ ns, Fig. 16. For the 1.06 μm radiation the radial size of the plasma pattern is about $r_f/2$ and the thermal radiation flux q_z is nonzero in this region only. For the 0.248 μm radiation q_z is greater and has a wider distribution, but in both cases the laser flux exceeds the thermal radiation flux over the entire irradiation zone. It was also established that after the end of the laser pulse the thermal radiation flux decreases rapidly and does not produce a significant effect.

Plasma emissivity is the quantity that characterizes the emission of the homogeneous plasma layer of thickness L, temperature T, and density ρ, $\varepsilon=\varepsilon(L,T,\rho)$: $q=\varepsilon\sigma T^4$. The numerical values of these characteristics $\varepsilon=q_{z,\max}/\sigma T_{\max}^4$

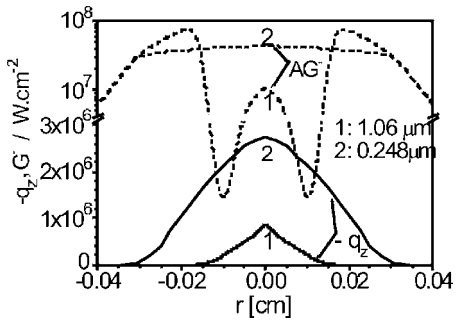

FIG. 16. Distributions at the target surface of the absorbed intensity of laser radiation $AG^-(t=25$ ns$,r,z=0)$ and the intensity of thermal radiation $-q_z(t=25$ ns$,r,z=0)$ for the laser wavelengths of 1.06 μm (curves 1) and 0.248 μm (curves 2), $G_0=5\times10^8$ W/cm^2, and $r_f=0.025$ cm.

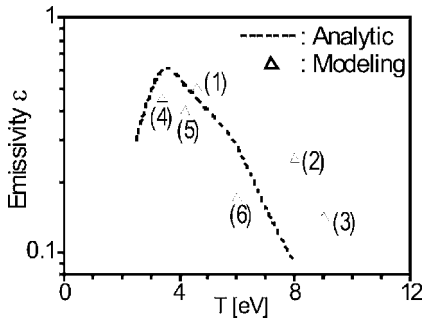

FIG. 17. Analytic emissivity of plasma layer taken from Ref. 41, Fig. 10(b), $L=0.03$ cm, $\rho=1.2\times10^{-3}$ g/cm^3, dashed line and calculated values of emissivity $\varepsilon=q_{z,\max}/\sigma T_{\max}{}^4$ (averaged over the period of time 20–30 ns) for the laser wavelength of 1.06 μm, (1) $G_0=5\times10^8$ W/cm^2, (2) 8×10^8 W/cm^2, (3) 10^9 W/cm^2, and 0.248 μm, (4) $G_0=5\times10^8$ W/cm^2, (5) 8×10^8 W/cm^2, and (6) 10^9 W/cm^2, $r_f=0.025$ cm.

(averaged over the period of 20–30 ns) are shown in Fig. 17 by triangles for the 1.06 μm radiation, $G_0=(5,8,\text{and }10)\times10^8$ W/cm^2, points (1), (2), and (3) and the 0.248 μm, $G_0=(5,8,\text{and }10)\times10^8$ W/cm^2, points (4), (5), and (6). The analytic dependence (dotted line) is taken from Ref. 41 [Fig. 10(b)] for the parameters $L=0.03$ cm and $\rho=1.2\times10^{-3}$ g/cm^3 which are representative for the plasma pattern shown in Fig. 15, plots T and ρ. The numerical and analytic values are in reasonable agreement, in particular, the tendency of the emissivity to decrease with increasing temperature is clearly seen. As it was established by modeling, the total radiative energy loss is 3%–6% of the accumulated plasma energy during the laser pulse and approximately as much at the stage of the inertial expansion and cooling.

V. COMPARISON WITH EXPERIMENT AND DISCUSSION

In the previous sections some experimental results were already mentioned which were found to be qualitatively consistent with the numerical predictions. In this section a more accurate comparison is performed dealing with the threshold laser intensity of the plasma formation (Sec. V A) and the thickness of the removed layer (Sec. V B). Also some considerations are given as to how the found regularities depend on the target material and environment parameters (Sec. V C).

A. Threshold intensities of plasma formation

Threshold intensity of the nanosecond laser irradiation of an aluminum target in vacuum leading to the plasma formation was measured in Refs. 55 and 61–65. The plasma initiation was identified by means of either the pattern emission or a sharp increase of the ion flux. The used action parameters and the found threshold values are presented in Table I, rows 1–4. Row 5 presents the threshold intensities predicted numerically for the same action parameters by using the condition of the electron-ion collision domination over the electron-neutral ones $\nu_{ei}>\nu_{en}$ as the criteria of the plasma formation.[4,66] The numerical results underestimate the experimental values in most of the cases, but the trend of the two dependencies is the same: the threshold intensity lowers down with the wavelength decreasing.[32,33,66] A more detailed comparison is not expedient first of all because of the different criteria of the plasma formation. The inaccuracy of the model is also explained by the application of the equilibrium description for the plasma formation phenomenon (optical breakdown). A more correct determination of the threshold intensities is possible by means of a kinetic model of nonequilibrium plasma[32,66] coupled with the expansion gas dynamics.

TABLE I. Comparison of the experimentally measured threshold intensities for the vapor plasma formation with the numerically predicted values.

Wavelength (μm)	1.06	0.532	0.355	0.308		0.248	
Reference	62	63	63	55	61	64	65
Pulse duration (ns)	7	6	6	20	20	15	17
Threshold intensity (experiment) (10^8 W/cm^2)	14	3.8	3.0	2.0	2.2	1.15	1.85
Threshold intensity (modeling) (10^8 W/cm^2)	10	4.3	2.9	1.1	1.1	1.2	1.25

The spectral dependence of the threshold intensity $G^*(\lambda)$ predicted for the fixed duration of the laser pulse $\tau=20$ ns is presented in Table II. The intensity begins to decrease approximately at the boundary of the visible spectrum. In particular, the threshold value for the 1.06 μm Nd:YAG laser is approximately three times higher than the one for the lasers of the UV range.

B. Removed layer thickness

The mean thickness of the removed layer is likely the most often analyzed quantity in the experimental and numerical studies of the laser ablation. In this subsection experimental results on the nanosecond laser ablation of aluminum in vacuum at different wavelengths are used.[17,55,65,67] In the modeling the following four parameters of the laser effect were taken approximately the same as in the experiments: laser wavelength, peak intensity, pulse duration, and beam radius.

Lasers of 1.06 and 0.532 μm. An experimental study of evaporation in vacuum for a number of materials induced by the 1.06 μm laser with the peak intensity of 10^8–5×10^9 W/cm^2, the pulse duration of 30 ns, and the beam radius of 20–250 μm was performed in Ref. 17. It was established that for the group of metals (Ti, Al, and W) and the

TABLE II. The predicted values of the threshold intensities for the vapor plasma formation for the different values of laser wavelength and the fixed pulse duration of 20 ns.

Laser	Nd:YAG	Ga–As	Ruby	HeNe	Nd:YAG	XeF	XeCl	KrF	ArF
Wavelength (μm)	1.06	0.9	0.694	0.639	0.532	0.351	0.308	0.248	0.193
Threshold intensity G^* (10^8 W/cm)	2.6	2.6	2.5	2.4	2.15	1.65	1	1.05	1

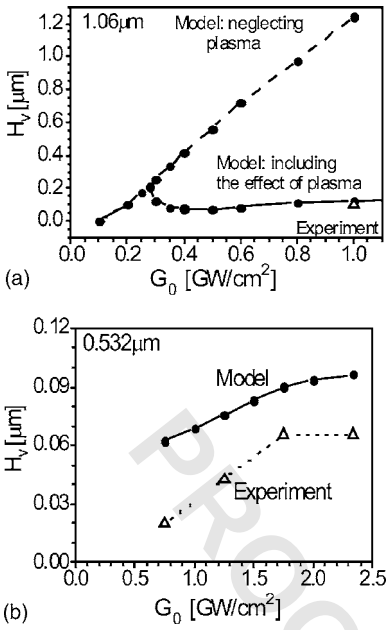

FIG. 18. Removed layer thickness vs laser intensity $H_v(G_0)$ predicted numerically with the account for the effect of plasma (solid lines), neglecting plasma (dashed lines), or found experimentally (triangles) (Refs. 17, 46, and 67) for the laser wavelengths of (a) 1.06 μm and (b) 0.532 μm and r_f =0.025 cm.

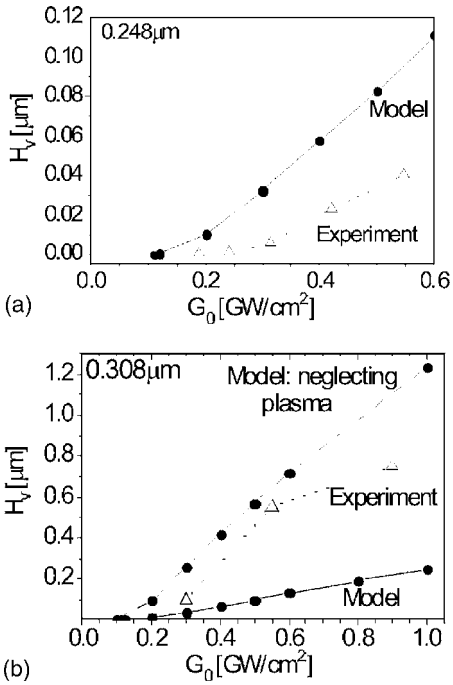

FIG. 19. Removed layer thickness vs laser intensity $H_v(G_0)$ predicted numerically and found experimentally for the laser wavelengths of (a) 0.248 μm (Ref. 65) and (b) 0.308 μm (Ref. 55).

laser intensity greater than 5×10^8 W/cm^2 the thickness of the removed layer was approximately constant and lied in the range of 0.05–0.1 μm. The particular value for Al (Refs. 17 and 46) for the intensity of 10^9 W/cm^2 was about 0.1 μm, Fig. 18(a), triangle. The solid curve in the same figure shows the numerical dependence of the removed layer predicted by the model: the thickness increases for the subthreshold intensities, sharply decreases, passes through minimum, and then demonstrates a slow increase with a much lower slope in comparison with the preplasma regime. The particular result for the intensity of 10^9 W/cm^2 is somewhat greater than the experimental value. The same figure shows the dependence $H_v(G_0)$ predicted without account for the plasma effect, Fig. 18(a), dashed line: the thickness increases monotonically and with constant rate over the entire range of intensities, exceeding the experimental value by more than an order of magnitude.

Experimental data for the 0.532 μm Nd:YAG laser of the visible range with the peak intensity of (0.7–2.4) $\times10^9$ W/cm^2, the pulse duration of 6 ns, and the beam radius of 0.06 cm are marked by triangles in Fig. 18(b).[67] The removed layer thickness first increases and then approaches the constant level of about 0.06 μm. The numerical dependence, solid line, demonstrates a similar behavior but gives values overestimated by a factor of 1.5-3.

Lasers 0.248 and 0.308 μm. While analyzing the thickness of the layer removed by UV laser radiation, an additional complexity arises from the injection of macroparticles from the target surface.[4,68] The contribution of this mechanism to the total mass removal can be substantially reduced if the target is rotated between the subsequent laser pulses and thus the irradiated spot is shifted partially or completely to a virgin part of the surface. It was pointed out in Refs. 65 and 68 that by applying the target rotation technique the removed mass occasionally decreased by a factor of 5–10.

Triangles in Fig. 19(a) correspond to the results of Ref. 65 analyzing the 0.248 μm KrF laser radiation with the peak intensity of 10^8–10^9 W/cm^2, the pulse duration of 17 ns, and the spot size of 0.1×0.05 cm^2. In the experiment the target was rotated after every shot providing the shift of 0.035 cm. The removed layer thickness was evaluated as $H_v=M(N\rho s)$, where M is the total removed mass determined by weighing, N is the number of shots, and ρ is the target density. Despite the plasma formation, the removed layer thickness grows monotonically with the increase in intensity. The numerical predictions, Fig. 19(a), solid line, have the same trend but are greater than experimental data by two to three times.

The alternative setup of experiment was used in Refs. 4 and 55 for the 0.308 μm XeCl laser with the intensity range of 10^8–10^9 W/cm^2, the pulse duration of 20 ns, and the beam radius of 0.025 cm: the target was not rotated and the removed layer thickness per shot was calculated as the total depth of the hollow divided by the number of pulses. The obtained results were within a range of 0.1–1 μm, Fig. 19(b), triangles, i.e., an order of magnitude higher than the results for the "rotational" setup, Figs. 19(a). The results predicted numerically with the same laser parameters do not exceed 0.2 μm, Fig. 19(b), solid line. The predictions of the model in which the plasma effect was neglected are also shown by dashed line and, as it is seen, this curve lies much closer to the experimental dependence. This coincidence, however, is purely occasional and results from the codirectional effect of two factors: the contribution of the thermal evaporation greatly overestimated due to the neglected

plasma effect is compensated by the contribution of the nonthermal mechanism of removal in the experimental values.

Summarizing, the comparison of numerical results with experimental data for the removed layer thickness demonstrated that the model correctly predicts trends for dependencies on radiation intensity, an accounting of the plasma effect is necessary for the correct estimation of the thermal mechanism contribution, and while analyzing experimental data on the UV laser radiation the other nonthermal mechanisms of removal have to be accounted for. One of the major reasons of the quantitative deviation is likely a great uncertainty of the target parameters used in the model at high temperature.

C. Dependence on the target material and environment parameters

The regularities considered in the previous sections are related to the laser irradiation of an aluminum target in vacuum. Below some qualitative considerations are presented regarding to what extent these regularities can manifest themselves with other target materials and for the ablation in air or inert gas environment.

Numerical studies of the laser-induced phenomena involving the formation of vapor plasma often deal with only one material, e.g., aluminum[30,32,37,41–43] or copper.[23,28] It is explained by the complexity of calculation of the plasma properties, first of all its charge composition and absorption coefficient. Experimentally, the influence of the target material properties on laser evaporation and vapor plasma induced by the nanosecond Nd:YAG and ruby laser radiation with the intensity of about 10^9 W/cm^2 in vacuum was studied in Refs. 17 and 46. It was established that the considered materials can be divided into two groups characterized by essentially different values of the threshold intensity of plasma formation, the thickness of the ablated layer as well as by the structure and the expansion regime of the plasma pattern. The explanation in Ref. 17 is that for the materials of the first group that includes Ti, Al, W, and some other metals the plasma is formed in the evaporated substance before the condition of thermodynamic instability $T > 0.9T_{crit}$ is reached on the surface. On the other hand, this condition is likely realized for the materials of the second group (Bi, Pb, Ge, Si) leading to the explosivelike decay of the overheated metastable phase[5] and, consequently, to a much higher mass removal. Our numerical predictions for Al are consistent with the features of the first group (see Sec. III B), and thus one may suppose that the effect of the plasma on evaporation for other metals of the first group will be similar to the one established for aluminum for lasers operating in the near-IR and visible spectral range.

If laser ablation is performed in air or inert gas (He and Ar) environment at the typical pressure of 1 atm, the description of the process becomes more complex and has to account for the formation of the shock wave and plasma in the gas, diffusion, heat conduction, and recombination heating.[51,69] From the point of view of the surface phase transition, the main distinction consists in the occasional formation of a second plasma in the environmental gas that might contribute to attenuation of the incident laser flux, generation of the counterpressure, and emission of the thermal radiation. As a consequence, an accurate analysis of the phenomena has to be performed separately for every pair of the target material and environmental gas. The analysis of the Cu ablation in a chamber filled by He at the pressure of 1 atm showed[23] that the principal characteristics of the surface (temperature, counter-pressure, direction of the phase transition, and removed layer thickness) are rather similar to the ones of this study and are controlled by the vapor plasma located in the near-surface region, while the plasma of He remains rather cold and transparent.

VI. CONCLUSION

The performed study allowed us to establish the following features of the phase transitions on the surface of an aluminum target and vapor plasma induced by the nanosecond radiation of the 1.06 and 0.248 μm lasers with the intensity of 10^8–10^9 W/cm^2.

- The 1.06 μm irradiation leads to the formation of an optically dense plasma with the temperature of 5–10 eV that prevents further target heating. The evaporation stops but can occasionally resume at the final stage of the pulse. The evaporation proceeds nonuniformly in the spot area; the major contribution to mass removal occurs in the outer part of the spot above which the plasma is not formed and the sonic evaporation persists until the end of the action.
- The 0.248 μm laser plasma forms just at once after the beginning of the evaporation over all the spot area but remains colder and partially transparent transmitting 30%–70% of the incident radiation; therefore the evaporation does not stop but continues in the subsonic regime with the Mach number of about 0.1 retarded by the high counterpressure of the near-surface plasma layer.
- For the 1.06 μm radiation, 15%–20% of the total of the evaporated matter condenses back to the surface during the laser pulse in consequence of the plasma counterpressure. For the UV radiation the condensation is weaker, proceeds after the end of the pulses, the condensed fraction grows with the beam radius increasing but does not exceed 10%.
- For the beam radius smaller than $\sim$100 μm the screening and retarding effect of the plasma weakens due to the lateral expansion, the thickness of the removed layer increases, and condensation after the end of the pulse does not occur.
- The structure, the shape, and the expansion regime of the plasma pattern induced by irradiation at different wavelengths have a number of distinctions; the contribution of the thermal plasma radiation and its effect on the target is much weaker than the ones of the laser radiation.
- The comparison of numerical and experimental data for the removed layer thickness demonstrated that the model correctly predicts trends for dependencies on radiation intensity and showed the importance of accounting for the plasma effect.

[1] M. Von Allmen, *Laser-Beam Interactions with Materials* (Springer-Verlag, Berlin, 1987).
[2] S. M. Metev and V. P. Veiko, *Laser-Assisted Microtechnologies* (Springer-Verlag, Berlin, 1998).
[3] R. E. Russo, X. Mao, and S. S. Mao, Anal. Chem. **74**, 70A (2002).
[4] A. Gorbunov, *Laser-Assisted Synthesis of Nanostructured Materials* (VDI, Dusseldorf, 2002).
[5] A. A. Samokhin, in *Effect of Laser Radiation on Absorbing Condensed Matter*, Proceedings of the General Physics Institute USSR Academy of Sciences, edited by A. V. Prokhorov (Nova Science, New York, 1990), Vol. 13.
[6] G. S. Romanov and V. K. Pustovalov, Izv. Akad. Nauk SSR Ser. Fiz. Mat. Nauk ■, 84 (1967).
[7] S. I. Anisimov, Sov. Phys. JETP **27**, 182 (1968).
[8] Ch. J. Knight, AIAA J. **17**, 519 (1979).
[9] A. A. Samokhin, Kratk. Soobshch. Fiz. ■, 3 (1982).
[10] B. Ya. Moizhes and V. A. Nemchinskii, Zh. Tekh. Fiz. **52**, 684 (1982).
[11] M. Aden, E. Beyer, G. Herziger, and H. Kunze, J. Phys. D **25**, 57 (1992).
[12] P. V. Breslavskii and V. I. Mazhukin, Report No. 2 (VTcMM RAN, Moscow, 1992).
[13] S. H. Jeong, R. Greif, and R. E. Russo, Appl. Surf. Sci. **127–129**, 177 (1998).
[14] A. V. Gusarov and I. Smurov, J. Appl. Phys. **97**, 014307 (2005).
[15] Ch. J. Knight, AIAA J. **20**, 950 (1982).
[16] V. I. Mazhukin and A. A. Samokhin, Sov. J. Quantum Electron. **14**, 1608 (1984).
[17] V. I. Luchin, Izv. Vyssh. Uchebn. Zaved., Radiofiz. **23**, 177 (1980).
[18] R. Kelly and A. Miotello, Appl. Surf. Sci. **96–98**, 205 (1996).
[19] J. H. Yoo, S. H. Jeong, R. Greif, and R. E. Russo, J. Appl. Phys. **88**, 1638 (2000).
[20] Yu. V. Afanas'ev and O. N. Krokhin, in *The Physics of High Energy Densities*, edited by P. Caldirola and H. Knoepfel (Academic, New York, 1974).
[21] R. Kelly and B. Braren, Appl. Phys. B: Photophys. Laser Chem. **53**, 160 (1991).
[22] R. Kelly and A. Miotello, Nucl. Instrum. Methods Phys. Res. B **91**, 682 (1994).
[23] Z. Chen and A. Bogaert, J. Appl. Phys. **97**, 063305 (2005).
[24] A. A. Morozov, Appl. Surf. Sci. **252**, 2978 (2006).
[25] K. Aoki, Y. Sone, and T. Yamada, Phys. Fluids A **2**, 1867 (1990).
[26] Y. Sone, S. Takata, and F. Golse, Phys. Fluids **13**, 324 (2001).
[27] V. I. Bergel'son and I. V. Nemtchinov, Sov. J. Quantum Electron. **8**, 1198 (1978).
[28] A. Vertes, R. W. Dreyfus, and D. E. Platt, IBM J. Res. Dev. **38**, 1 (1994).
[29] G. S. Romanov and Yu. A. Stankevich, Fiz. Khim. Obrab. Mater. **2**, 15 (1981).
[30] V. I. Zubov, V. M. Krivtsov, I. N. Naumova, and Yu. D. Shmyglevskii, Zh. Vychisl. Mat. Mat. Fiz. **23**, 1520 (1983).
[31] M. Aden, E. W. Kreutz, and A. Voss, J. Phys. D **25**, 1545 (1993).
[32] D. I. Rosen, J. Mitteldorf, G. Kothandaraman, A. N. Pirri, and E. R. Pugh, J. Appl. Phys. **53**, 3190 (1982).
[33] A. M. Popov, O. B. Popovicheva, and T. V. Rakhimova, Fiz. Plazmy **11**, 370 (1988).
[34] I. Horn, M. Guillong, and D. Gunther, Appl. Surf. Sci. **182**, 91 (2001).
[35] V. I. Mazhukin, V. V. Nossov, and I. Smurov, J. Appl. Phys. **90**, 607 (2001).
[36] V. I. Mazhukin and G. A. Pestryakova, Dokl. Akad. Nauk SSSR **278**, 843 (1984).
[37] V. I. Mazhukin, V. V. Nossov, and I. Smurov, Thin Solid Films **453–454**, 353 (2004).
[38] V. I. Mazhukin and V. V. Nossov, IEEE J. Quantum Electron. **35**, 454 (2005).
[39] V. I. Bergelson and I. V. Nemtchinov, Sov. J. Quantum Electron. **10**, 1373 (1980).
[40] V. I. Mazhukin, I. Smurov, and G. Flamant, J. Comput. Phys. **112**, 78 (1994).
[41] G. Weyl, J. Thermophys. Heat Transfer **8**, 229 (1994).
[42] J. R. Ho, C. P. Grogoropoulos, and J. A. C. Humphrey, J. Appl. Phys. **79**, 7205 (1996).
[43] V. I. Mazhukin, V. V. Nossov, I. Smurov, and G. Flamant, J. Phys. D **37**, 185 (2004).
[44] I. B. Gornushkin, A. Ya. Kazakov, N. Omenetto, B. W. Smith, and J. D. Winefordner, Spectrochim. Acta, Part B **59**, 401 (2004).
[45] G. Weyl, A. Pirri, and R. Root, AIAA J. **19**, 460 (1981).
[46] A. D. Aksakhalyan, S. V. Gaponov, V. I. Luchin, and A. P. Cherimanov, Sov. Phys. Tech. Phys. **33**, 1146 (1988).
[47] E. A. Volkova, A. C. Kovalev, A. M. Popov, and B. V. Seleznev, Sov. J. Quantum Electron. **20**, 200 (1990).
[48] H. S. Carslaw, and J. G. Jaeger, *Conduction of Heat in Solids* (Clarendon, Oxford, 1959).
[49] *Handbook of Physical Quantities*, edited by I. S. Grigoriev and E. Z. Meilikhov (CRC, New York, 1997).
[50] B. N. Chetveruskin, *Matematicheskoe Modelirovanie Dinamiki Izluchayushchego Gaza* (Nauka, Moscow, 1985).
[51] Ya. B. Zeldovich and Yu. P. Raizer, *Physics of Shock Waves and High Temperature Hydrodynamics Phenomena* (Academic, New York, 1966), Vols. I and II.
[52] N. N. Kalitkin, I. V. Ritus, and A. M. Mironov, Report No. 6 (IPM AN SSSR, Moscow, 1983).
[53] G. S. Romanov, K. L. Stepanov, and M. I. Sirkin, Opt. Spectrosc. **53**, 381 (1982).
[54] I. W. Boyd, *Laser Processing of Thin Films and Microstructures* (Springer-Verlag, Berlin, 1987).
[55] V. P. Ageev, A. A. Gorbunov, and V. I. Konov, Sov. J. Quantum Electron. **19**, 785 (1989).
[56] D. Crout, J. Math. Phys. **15**, 1 (1936).
[57] V. I. Mazhukin, P. A. Prudkovskii, and A. A. Samokhin, Mat. Model. **5**, 3 (1993).
[58] A. V. Gusarov and I. Smurov, Phys. Fluids **14**, 4242 (2002).
[59] A. A. Samarskii, *Teoriya Raznostnykh Skhem* (Nauka, Moscow, 1977).
[60] M. I. Volchinskaya, V. I. Mazhukin, B. N. Chetverushkin, and N. G. Churbanova, Zh. Vychisl. Mat. Mat. Fiz. **23**, 1177 (1983).
[61] D. V. Gaidarenko, A. G. Leonov, and D. I. Chekhov, Sov. J. Plasma Phys. **17**, 534 (1991).
[62] M. Ignatavichyus, E. Kazakavichyus, G. Orshevski, and V. Danyunas, Sov. J. Quantum Electron. **21**, 1210 (1991).
[63] S. Amoruso, A. Amodeo, V. Berardi, R. Bruzzesse, N. Spinelli, and R. Velotta, Appl. Surf. Sci. **96–98**, 175 (1996).
[64] J. E. Rothenberg and G. Koren, Appl. Phys. Lett. **44**, 664 (1984).
[65] R. Timm, P. R. Willmott, and J. R. Huber, J. Appl. Phys. **80**, 1794 (1996).
[66] V. I. Mazhukin, V. V. Nossov, M. G. Nikiforov, and I. Smurov, J. Appl. Phys. **93**, 56 (2003).
[67] A. Mele, A. Giardini Guidoni, R. Kelly, C. Flamini, and S. Orlando, Appl. Surf. Sci. **109–110**, 584 (1997).
[68] T. D. Bennett, C. P. Grigoropoulos, and D. J. Krajnovich, J. Appl. Phys. **77**, 849 (1995).
[69] H. C. Le, D. E. Zeitoun, J. D. Parisse, M. Sentis, and W. Marine, Phys. Rev. E **62**, 4152 (2000).